High speed laser tomography system

Samsonov, D.; Elsässer, A.K.G.; Edwards, A.; Thomas, H.; Morfill, G.

High speed laser tomography system

D. Samsonov, A. Elsaesser, A. Edwards, H. M. Thomas, and G. E. Morfill

Citation: Review of Scientific Instruments **79**, 035102 (2008); doi: 10.1063/1.2885683
View online: http://dx.doi.org/10.1063/1.2885683
View Table of Contents: http://aip.scitation.org/toc/rsi/79/3
Published by the American Institute of Physics

High speed laser tomography system

D. Samsonov,[1] A. Elsaesser,[1,a)] A. Edwards,[1] H. M. Thomas,[2] and G. E. Morfill[2]
[1]*Department of Electrical Engineering and Electronics, University of Liverpool, Brownlow Hill, L69 3GJ Liverpool, United Kingdom*
[2]*Max-Planck-Institut für Extraterrestrische Physik, 85741 Garching, Germany*

(Received 27 November 2007; accepted 4 February 2008; published online 7 March 2008)

A high speed laser tomography system was developed capable of acquiring three-dimensional (3D) images of optically thin clouds of moving micron-sized particles. It operates by parallel-shifting an illuminating laser sheet with a pair of galvanometer-driven mirrors and synchronously recording two-dimensional (2D) images of thin slices of the imaged volume. The maximum scanning speed achieved was 120 000 slices/s, sequences of 24 volume scans (up to 256 slices each) have been obtained. The 2D slices were stacked to form 3D images of the volume, then the positions of the particles were identified and followed in the consecutive scans. The system was used to image a complex plasma with particles moving at speeds up to cm/s. © *2008 American Institute of Physics.* [DOI: 10.1063/1.2885683]

I. INTRODUCTION

Tomography is an imaging method which reconstructs a three-dimensional (3D) image from two-dimensional (2D) sections or slices.[1] It is used in various disciplines of material science and medicine.[2–5] This technique is very popular due to its capability to create 3D images without destroying or invading the specimen.[6] Tomography has two well defined stages: 2D imaging and 3D image reconstruction. The 2D imaging can be performed using x-rays in computed tomography,[7] gamma rays in single photon emission computed tomography,[8] neutrons in neutron computed tomography,[5] positron electron annihilation reaction in positron emission tomography,[9] nuclear magnetic resonance in magnetic resonance imaging (MRI),[10,11] ultrasound in 3D ultrasonography,[12] light in optical coherence tomography,[13] electrons in 3D transmission electron microscopy,[14] and ions in atom probe tomography.[15] There are many image reconstruction algorithms,[9,16,17] most are relatively complex and computationally intensive, since they have to deal with continuous objects. The most widely used is the filtered back projection[18] which is an inversion of the Radon transform.[19] The Hough transform[20] is used for identifying lines, circles, and arbitrary shapes.

Dynamic and static diagnostic techniques are widely applied to the so-called mesoscale complex materials which include colloids, emulsions, granular media, foams, and complex plasmas. These techniques include optical imaging, x-ray tomography, MRI, and related structure and motion characterization algorithms. Optical imaging is typically done with a microscope coupled to a video camera.[21,22] Since microscopes have shallow depths of field, 3D views are acquired by shifting the focal plane. The resolution can be within 10 nm in the focal plane and 150 nm in depth at 30 slices/s. A more advanced technique is target-locking acquisition with real-time confocal microscopy.[23] It follows the target object using real-time data analysis algorithms. Another optical method speckle visibility spectroscopy[24] is based on dynamic light scattering. Its resolution is 10 nm and 50 μs using a line scan charge coupled device camera. Similar optical imaging techniques are used in biology. However, advanced tracking algorithms are required in order to select objects from a nonuniform background.[25,26] Structure of granular materials in 3D can be also reconstructed using x-ray microtomography,[22,27–29] a method that requires a synchrotron x-ray source. Submillimeter grains can be resolved at 1 s exposure time. Magnetic resonance imaging is used for granular media and foams[22,30] with 0.1 mm spatial and about 1 s time resolution.

Optical 3D laser scanners have been used widely to record shapes of large structures, such as tunnels[31] and for reverse engineering problems.[32] They operate by moving a laser beam across the object and recording the scattered light with a video camera. The data analysis procedure, which may involve a neural network, reconstructs the 3D trajectory of the laser beam and thus the shape of the scanned object.

The laser tomography system described here, was designed for imaging of complex plasmas, however, it can be used for other optically thin or translucent objects. Complex plasmas consist of plastic microspheres immersed in a low temperature ion-electron plasma.[33] These particles (or grains) charge up, levitate, and are confined in the gas discharge. Due to their high electric charge, they interact collectively and form ordered two-or three-dimensional structures.[34] Since the residual neutral gas provides low damping, a range of wave and dynamic phenomena can be observed.[35,36] These dynamic phenomena require good time resolution in order to trace the grains moving with speeds of up to a few cm/s.

3D diagnostics have been applied to complex plasmas in the past. In one experiment, the sample was illuminated by a thick laser beam with a color gradient created by mixing the light of two lasers.[37] This gradient was resolved with two

a)Present address: Centre for Molecular Bioscience, University of Ulster, Room W0044 Cromore Road, BT52 1SA Coleraine, United Kingdom.

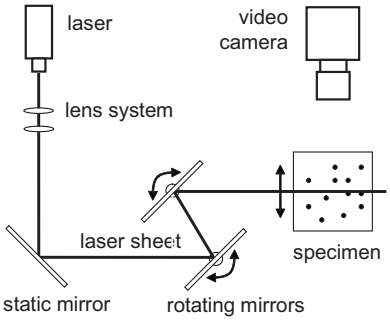

FIG. 1. Tomography system, side view. The laser sheet is formed by the cylindrical lenses. It is parallel shifted by two rotating mirrors to illuminate slices of the sample. The video camera records images of thin slices of the imaged volume.

video cameras and provided a measure of depth. Another method used two video cameras to produce stereoscopic images.[38] A third method employed a system which moved a laser sheet (a beam expanded with a line forming optics) with a translation stage to scan the sample and then reassembled the stack of 2D images.[34] The first and second systems are rather complicated from the experimental point of view and require significant computational efforts to reconstruct the 3D positions and velocities. The third system is slow and not synchronized with the video camera, and is therefore only useful in measuring static structures.

The tomography system proposed here performs fast scans of the imaged volume by parallel shifting a laser sheet with galvanometer-driven mirrors. A high speed digital video camera synchronously records the images of the scattered light, which are then recombined and a 3D structure of the sample computed.

II. TOMOGRAPHY SYSTEM

The tomography system comprises a 532 nm 300 mW Nd:yttrium aluminum garnet laser with a lens system, two rotating mirrors and a complementary metal-oxide semiconductor video camera (see Fig. 1). The laser beam is expanded into a 100 μm thick and 40–100 mm wide laser sheet by a cylindrical telescope. This laser sheet is deflected by a system of two galvanometer-driven mirrors which displace the laser sheet. To ensure that the beam is accurately parallel shifted, the mirrors rotate synchronously back and forth with an amplitude of several degrees and kept parallel to each other. The rotation axes of the mirrors are placed at the diagonal corners of a square with an edge length of 4 cm (Fig. 2). When the mirrors are in the neutral position, the laser sheet impinges on them at an angle of 22.5° to the normal. This is to achieve a linear (near the neutral position) dependence of the sheet height versus angular deflection of the mirrors.

The galvanometers move in microradian steps and the laser sheet is shifted in the vertical direction in steps of a few micrometers to millimeters. The step size should be less than the thickness of the illuminating laser sheet by a factor of 1.5–5 to avoid gaps in the images. The full scan height is up to 36 mm, limited by the size of the mirrors.

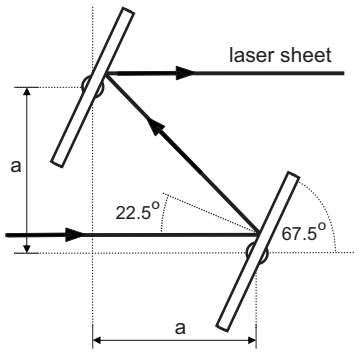

FIG. 2. Mirror setup. Two galvanometer driven mirrors placed on a diagonal of a square with the side $a=40$ mm rotate synchronously. The angle of incidence of the laser sheet in the neutral position is 22.5° to provide a linear response of the sheet position vs mirror deflection angle.

Since the scans can be performed with a different number of steps (NOS), we have to define a single step rate (SSR) and a full scan rate (FSR):

$$\mathrm{FSR} = \mathrm{SSR}/\mathrm{NOS},$$

where the number of steps is in the range between 2 and 256. The scans can be performed very fast. The single step rate, which is set by the frame rate of the camera, is adjustable up to 120 000 frames/s. This corresponds to 8 μs between the scan steps. We used a Photron ultima APX camera with frame rates of 50–2000 frames/s at full resolution of 1024 $\times$1024 pixels or up to 120 000 frames/s at reduced resolution.

In order to improve the dynamic characteristics of the scanning system, the mirrors are controlled by a triangular stepping signal (Fig. 3). Compared to a sawtooth control signal, this method does not require the mirrors to sweep a full range at the end of each scanning cycle. Because of their high inertia and slow high amplitude dynamic response, the mirrors would fail to complete the full range sweep in one scanning step at high scanning rates. This would result in uncertain mirror positions during the sweep. Ideally, the position of the laser sheet should remain constant during the exposure and make an instantaneous move between the frames.

The control unit (Fig. 4) generates a stepping signal synchronized with the video camera. A trigger signal from the camera (vertical sync signal gated with the record enable signal) is applied to the 8 bit reversible counter. The counting direction is controlled by a trigger which reverses when the lower or upper preset limit is reached. The counter output is converted by a digital to analog converter (DAC) and used

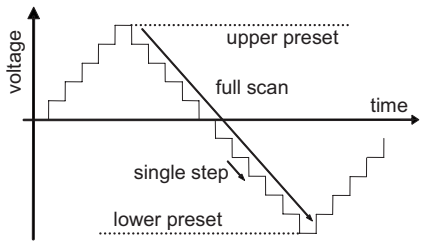

FIG. 3. Stepping signal. A triangular signal is used to prevent large amplitude motion of the mirrors in one step.

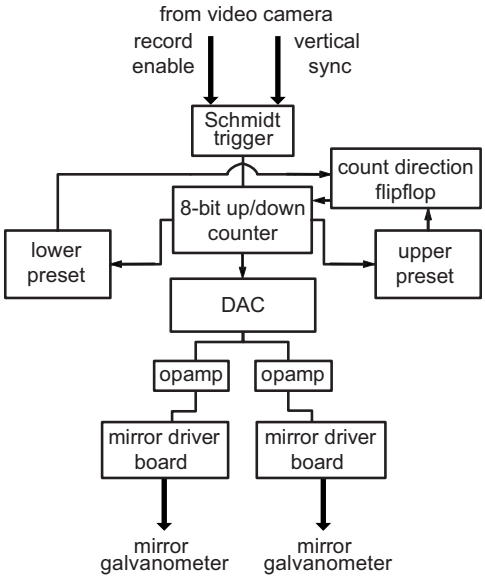

FIG. 4. Block diagram of the control unit. The vertical sync signal from the camera is applied to the reversible counter. Count direction is reversed when the count reaches the preset limits. The output of the counter is converted from digital to analog form to produce the stepping signal and used to drive the mirrors.

to drive the mirrors. The step size and fine mirror position adjustments for each channel are set by changing the gain and the offset of the output operational amplifiers separately.

III. SYSTEM CALIBRATION

In order to use the tomography system for measurements, it is necessary to know the position of the illuminating laser sheet as every frame is recorded. To determine the sheet position, we used an optical quality glass plate with a measurement grid of 0.48×0.48 mm^2 cells. The plate was placed on a goniometer at an angle of 10° to the sheet plane (Fig. 5). The laser light scattered from the glass plate was recorded with the video camera. The thickness and the vertical position of the laser sheet are calculated by multiplying the readings from the grid by the sine of the inclination angle (10°).

The recorded images of the measurement grid and the laser light scattered by the glass plate were analyzed by a computer program. The pixels in each row along the direction of the laser line were summed. Position and the thickness of the laser sheet were calculated using a Gaussian fit.

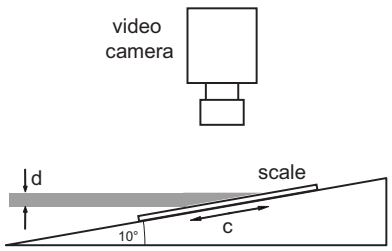

FIG. 5. Measurement of the laser sheet thickness and position. An inclined glass plate with a measurement grid is imaged by the video camera. The actual thickness of the laser sheet d is obtained from the measured value c using the formula $d=c \sin 10°$. The relative sheet position is obtained analogously.

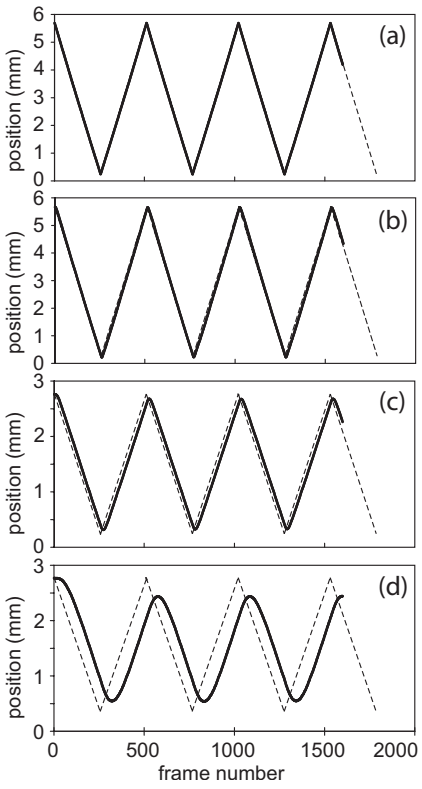

FIG. 6. Laser sheet position (solid line) vs frame number recorded at the frame rate of (a) 50 frames/s, (b) 2000 frames/s, (c) 10000 frames/s, (d) 40000 frames/s. The dashed line indicates the theoretical position for a massless mirror with instant response. As the frame rate increases, the actual mirror position is delayed due to the inertia. All scans are performed with 256 steps.

Figure 6 shows the laser sheet position versus time for different frame rates (single step rates) scanned with 256 steps. The dynamic performance of the tomographic scanning mechanism is very accurate at camera frame rates (equal to single step rate) up to 2000 frames/s. The deviation from the ideal mirror position (calculated for a massless mirror, as shown by the dashed line in Fig. 6) is less than 100 μm. At higher rates, the full scan amplitude decreases, the laser sheet position lags behind, and the inertia of the mirrors has to be included to calculate the true sheet position. The repeatability of the scans is very good at all scanning rates confirmed by tests of the system up to 120 000 frames/s. It should be noted that at high scanning rates, the position near the starting point [Fig. 6(d) near frame 0] are not repeated at the reversal point in the next scan (near frame 511); however, all the subsequent scans are identical.

IV. 3D IMAGE RECONSTRUCTION

The tomography system was designed to image micron-sized particles levitated in a gas discharge (or complex plasmas).[35,36] However, it can be used for any optically thin collection of fast moving pointlike objects such as particle seeded gas and fluid flows,[39,40] aerosols,[41] microbubbles,[42] bacteria,[43] etc.

In order to reconstruct the 3D images of the complex plasma, we stacked the 2D slices to form 3D volumes for

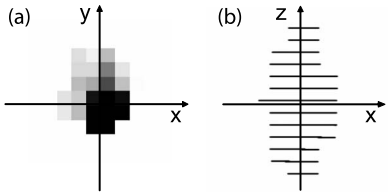

FIG. 7. Identification of particle positions. (a) First step: 2D positions are calculated in each slice as intensity weighted moments of pixel positions (pixel brightness is inverted). (b) Second step: the third coordinate is determined from a stack of slices as intensity weighted moments of particle positions in the slices.

each full scan. The 3D particle coordinates were obtained by adapting 2D particle identification subroutines written in interactive data language. The particles appear in 2D slices as bright spots several pixels in diameter [Fig. 7(a)]. Their 2D horizontal positions were calculated in each slice as intensity weighted moments of pixel positions after thresholding the images.[44] The scanning step was selected smaller than the thickness of the illuminating laser sheet, so that the grains appeared in several adjacent slices. The third vertical coordinate was determined as the intensity weighted moment of the particle positions in the slices [Fig. 7(b)]. It was assumed that the grain displacements were small in the several neighboring slices, the particle velocities were then determined by identifying particles in consecutive scans (assuming that the displacements were smaller than the distances between the grains).

V. COMPLEX PLASMA EXPERIMENTS

The tomography system was tested in a real complex plasma experiment which was performed in a rf-discharge plasma chamber (Fig. 8) with the lower disk electrode measuring about 20 cm in diameter. The chamber served as the other grounded electrode. A pressure of 1.420 Pa was maintained by the argon gas flow at a rate of 4 SCCM (SCCM denotes cubic centimeter per minute at STP). A radio frequency (rf) power of 1 W at 13.56 MHz was applied to the lower electrode. The induced −7 V dc self-bias of the powered electrode with respect to the ground depends on the ratio of the electrode areas. The self-bias voltage creates an electric field in the sheath region, that is strong enough to levitate negatively charged grains. The grains acquire high negative charges (analogously to floating Langmuir probes) when they are immersed in a plasma, electron photoemission is negligible.

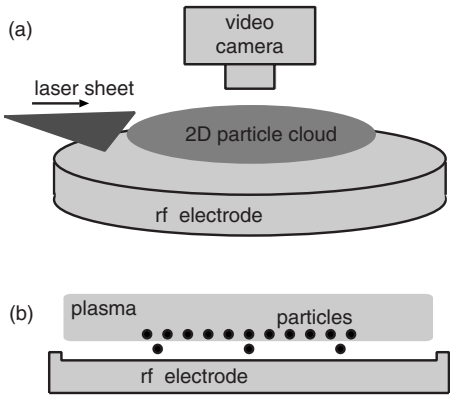

FIG. 8. Complex plasma experiment. (a) Oblique view of the experimental setup (the vacuum chamber is not shown). (b) Side view. The particles levitate in the sheath region of the plasma. A crystalline monolayer is formed of 9.19 μm microspheres. A few 21.83 μm grains levitate 1–2 mm below the main layer moving with speeds of up to 16 mm/s.

Monodisperse plastic microspheres of two diameters 9.19 and 21.83 μm were immersed in the discharge and levitated in the sheath above the rf electrode. The smaller particles formed an almost stationary monolayer hexagonal crystalline structure with the average interparticle separation in the horizontal plane of about 1 mm. The standard deviation of the vertical coordinate was 25 μm, which is at the limit of the vertical resolution. A few larger particles levitated 1–2 mm below the main layer moving around at speeds of up to 16 mm/s.

The complex plasma was scanned at 1000 frames/s using 128 step scans which corresponded to 7.8125 Hz full scan rate. With the step size of 29.07 μm, the full scan amplitude was 3.72 mm. The images had a resolution in the horizontal direction of 1024×1024 pixels at 26.93 μm/pixel. Figures 9(a)–9(c) shows a 3D reconstruction of the complex plasma, the particles are black dots. Their positions were then identified by the software (highlighted by red circles). The main crystalline layer of particles appears to be very thin. Figures 9(d)–9(f) shows identified positions of the bigger grains (with the main layer of small particles removed) which were moving below the monolayer. They are plotted with different colors corresponding to the scan number. We recorded eight full scans and followed the particles for a time period of 1.024 s. The maximum grain displacement was about 3 mm which corresponds to a speed of 16 mm/s. This showed the capability of the system to trace the movements of the particles.

VI. DISCUSSION

The tomography system performed well producing reliable and repeatable results. Here, we will discuss methods to further improve the performance and capabilities of the system. Most of the limitations are due to the components used and not imposed by the fundamental laws of nature.

The tomography system produces sequences of scans (2–256 slices each adjustable in increments of 1) of the the imaged volume. It is easily possible to increase the number of steps by adding more counters to the control unit thereby increasing resolution. The step size can be set in the range from microns to millimeters; however, the full scan amplitude should not exceed 36 mm (this value depends of the size of the moving mirrors used). The scanning rate is determined by the frame rate of the video camera used. We tested the system with scanning rates ranging from 50 to steps/s. The scanning rate can be further increased by using smaller and lighter galvanometer mirrors reducing their inertia and increasing the angular speed.

The system had a horizontal resolution of about 10–40 μm/pixel and a depth of field of 1.5–6 mm, these

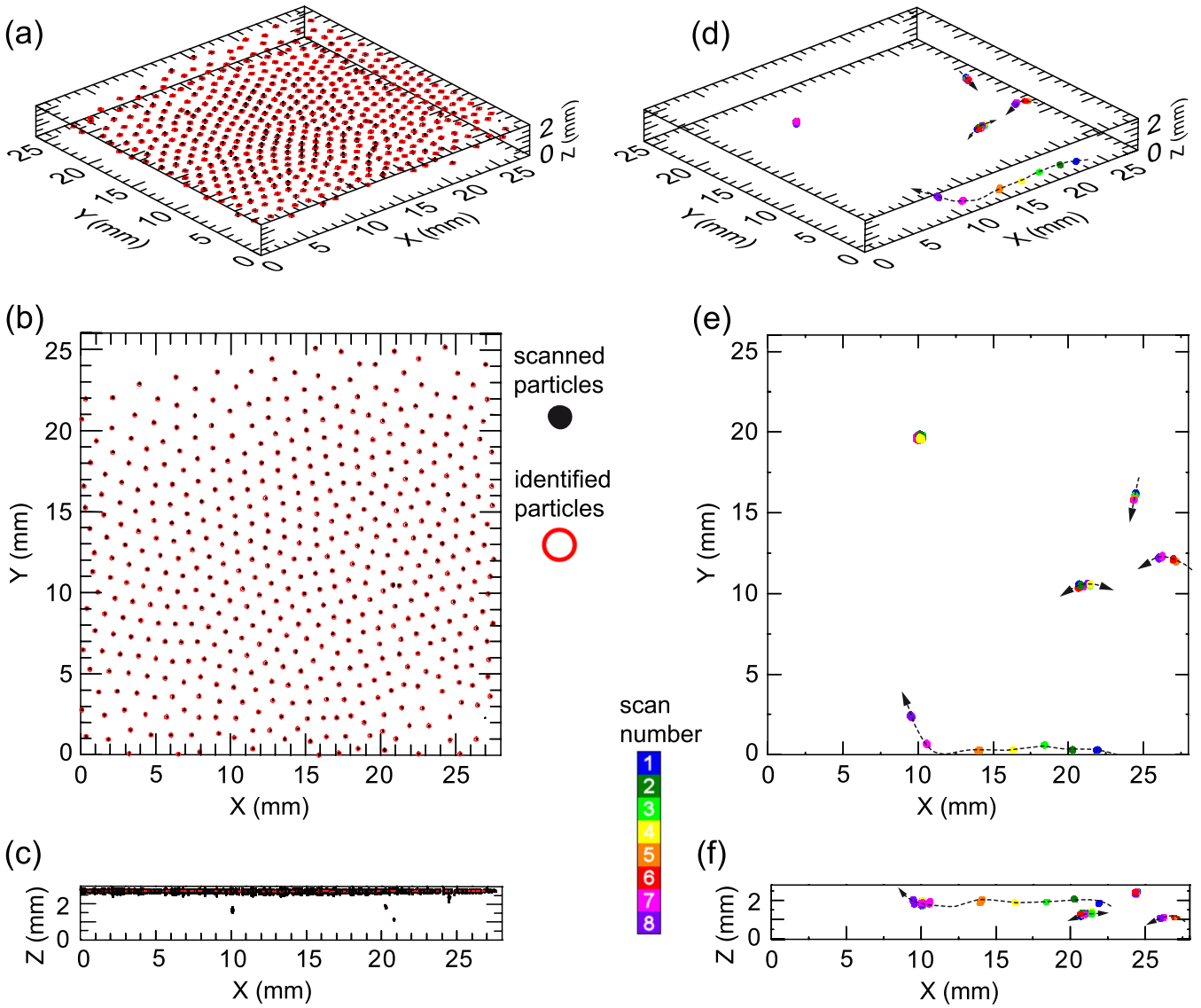

FIG. 9. (Color online) Experimental observation of the complex plasma. The stacked 2D slices are shown in black color in the (a) oblique, (b) top, and (c) side view of a single 3D scan. Red circles mark particles identified by the software. The main layer has crystalline structure. The heavier particles in the (d) oblique, (e) top, and (f) side views levitate 1–2 mm below and move at up to 16 mm/s. The color of the particles indicates the scan number in the series of eight scans. The trajectories are shown by the dashed lines with arrows pointing the directions of motion.

parameters depend on the camera lens and the distance from the imaging volume. The depth of field depends on the aperture of the lens. The smaller the aperture, the higher the depth of field. However, smaller apertures admit less light and thus might cause underexposure. Choosing a more sensitive video camera and a more powerful illuminating laser will enhance system performance; however, an overly powerful laser might affect the grain motion due to its light pressure.

The thickness of the illuminating laser sheet which determines the vertical resolution was chosen to be 100 μm. The sheet near the field zone covered a length of 120 mm. Decreasing the thickness of the illuminating sheet will enhance the vertical resolution at the expense of smaller field of view. The sheet width was adjustable in the range of 40 to 100 mm. This is enough to provide uniform illumination over the maximum field of view of about 50×50 mm^2 with little falloff at the edges. The use of raster optics line generator instead of the cylindrical lenses will improve illumination uniformity even further.

VII. CONCLUSION

The high speed laser tomography system was developed for 3D imaging of complex plasmas or for any optically thin cloud of micron-sized particles. It utilizes simple software algorithms to produce 3D scans and to identify positions of particles. It can be used for particle tracking velocimetry to determine the velocities of individual grains.

The tomography system has proved to be reliable, easy to synchronize with external events, and straightforward to operate. The algorithms for 3D reconstruction, particle identification and tracking are not computationally intensive and

easy to implement. The optical and mechanical parameters of the system are mostly limited by the components used and thus can be further improved.

Compared to the previous achievents in 3D imaging of colloids, granular media, and foams,[21–30] the developed system significantly improves the spatial and time resolution as well as the size of the imaged volume.

ACKNOWLEDGMENTS

This work was supported by the Department of Electrical Engineering and Electronics at the University of Liverpool and by the Max-Planck Institute for extraterrestrial Physics, Garching.

[1] *Tomography* (http://en.wikipedia.org/wiki/Tomography).
[2] J. Peterson, L. Bancroft, and M. Kransdorf, Eur. J. Radiol. **56**, 319 (2005).
[3] M. Defrise and G. Gullberg, Phys. Med. Biol. **51**, R139 (2006).
[4] R. Bates, K. Garden, and T. Peters, Proc. IEEE **71**, 0300 (1983).
[5] B. Schillinger, E. Lehmann, and P. Vontobel, Physica B **276–278**, 59 (2000).
[6] A. Sinha, P. Sarkar, Y. Kashyap, and B. Godwal, Insight **45**, 59 (2003).
[7] C. K. Zoltani, K. J. White, and F. A. D. Bianca, Rev. Sci. Instrum. **57**, 602 (1986).
[8] S. Webb, A. P. Long, R. J. Ott, M. O. Leach, and M. A. Flower, Med. Phys. **12**, 53 (1985).
[9] M. A. Abidi and P. B. Davis, Opt. Eng. (Bellingham) **29**, 567 (1990).
[10] R. Damadian, Science **171**, 1151 (1971).
[11] W. S. Hinshaw, J. Appl. Phys. **47**, 3709 (1976).
[12] F. Mao, J. Gill, D. Downey, and A. Fenster, Med. Phys. **27**, 1961 (2000).
[13] J. R. Singer, F. A. Grünbaum, P. Kohn, and J. P. Zubelli, Science **248**, 990 (1990).
[14] A. Ourmazd, K. Ahlborn, K. Ibeh, and T. Honda, Appl. Phys. Lett. **47**, 685 (1985).
[15] T. F. Kelly and M. K. Miller, Rev. Sci. Instrum. **78**, 031101 (2007).
[16] H. E. Cline, W. E. Lorensen, S. Ludke, C. R. Crawford, and B. C. Teeter, Med. Phys. **15**, 320 (1988).
[17] G. M. D'Ariano, C. Macchiavello, and M. G. A. Paris, Phys. Rev. A **50**, 4298 (1994).
[18] U. van Stevendaal, J.-P. Schlomka, A. Harding, and M. Grass, Med. Phys. **30**, 2465 (2003).
[19] V. V. Kotlyar and A. A. Kovalev, Opt. Eng. (Bellingham) **45**, 078201 (2006).
[20] O. O. Ogundana, C. R. Coggrave, R. L. Burguete, and J. M. Huntley, Opt. Eng. (Bellingham) **46**, 051002 (2007).
[21] J. C. Crocker and D. G. Grier, J. Colloid Interface Sci. **179**, 298 (1996).
[22] D. Mueth, G. Debregeas, G. Karczmar, P. Eng, S. Nagel, and H. Jaeger, Nature (London) **406**, 385 (2000).
[23] P. Lu, P. Sims, H. Oki, J. Macarthur, and D. Weitz, Opt. Express **15**, 8702 (2007).
[24] P. Dixon and D. Durian, Phys. Rev. Lett. **90**, 184302 (2003).
[25] S. Rogers, T. Waigh, X. Zhao, and J. Lu, Phys. Biol. **4**, 220 (2007).
[26] Y. Kalaidzidis, J. Cell Biol. **86**, 569 (2007).
[27] G. T. Seidler, G. Martinez, L. H. Seeley, K. H. Kim, E. A. Behne, S. Zaranek, B. D. Chapman, S. M. Heald, and D. L. Brewe, Phys. Rev. E **62**, 8175 (2000).
[28] P. Richard, P. Philippe, F. Barbe, S. Bourles, X. Thibault, and D. Bideau, Phys. Rev. E **68**, 020301 (2003).
[29] K. Thompson, C. Willson, and W. Zhang, Powder Technol. **163**, 169 (2006).
[30] C. Gonatas, J. Leigh, A. Yodh, J. Glazier, and B. Prause, Phys. Rev. Lett. **75**, 573 (1995).
[31] R. Wissler and C. Froehlich, Proc. SPIE **2249**, 96 (1994).
[32] V. H. Chan, C. H. Bradley, and G. W. Vickers, Proc. SPIE **3204**, 156 (1997).
[33] H. Thomas and G. Morfill, Nature (London) **379**, 806 (1996).
[34] J. Pieper, J. Goree, and R. Quinn, Phys. Rev. E **54**, 5636 (1996).
[35] D. Samsonov, G. Morfill, H. Thomas, T. Hagl, H. Rothermel, V. Fortov, A. Lipaev, V. Molotkov, A. Nefedov, O. Petrov, A. Ivanov, and S. Krikalev, Phys. Rev. E **67**, 036404 (2003).
[36] D. Samsonov, S. Zhdanov, and G. Morfill, Phys. Rev. E **71**, 026410 (2005).
[37] T. Antonova, B. M. Annaratone, D. D. Goldbeck, V. Yaroshenko, H. M. Thomas, and G. E. Morfill, Phys. Rev. Lett. **96**, 115001 (2006).
[38] E. Thomas, Jr., J. D. Williams, and J. Silver, Phys. Plasmas **11**, L37 (2004).
[39] T. S. Yang and S. S. Shy, Phys. Fluids **15**, 868 (2003).
[40] R. J. E. Walpot, C. W. M. van der Geld, and J. G. M. Kuerten, Phys. Fluids **19**, 045102 (2007).
[41] R. J. Calhoun, R. Heap, J. Sommer, M. Princevac, J. Peccia, and H. Fernando, Proc. SPIE **5403**, 683 (2004).
[42] J. H. Xu, S. W. Li, Y. J. Wang, and G. S. Luo, Appl. Phys. Lett. **88**, 133506 (2006).
[43] M. F. Gluch, R. Gatz, and W. Baumeister, Rev. Sci. Instrum. **65**, 3866 (1994).
[44] Y. Feng, J. Goree, and B. Liu, Rev. Sci. Instrum. **78**, 053704 (2007).